Multi-core-shell nanoboxes comprising polydopamine-derived C coated NiCo@C and FeCo@C nanohybrid for enhanced electrochemical quantification of nitrofurantoin

Peer-reviewed author version

Shui, Xiaojuan; Ma, Huimin; Zhang , Yuanyuan; Zeng, Ting; Yang , Juan; Wu, Zhen; Zhang , Xiuhua & YANG, Nianjun (2024) Multi-core-shell nanoboxes comprising polydopamine-derived C coated NiCo@C and FeCo@C nanohybrid for enhanced electrochemical quantification of nitrofurantoin. In: Chemical engineering journal, 500 (Art N° 156714).

DOI: 10.1016/j.cej.2024.156714
Handle: http://hdl.handle.net/1942/44628

Multi-core-shell nanoboxes comprising polydopamine-derived C coated NiCo@C and FeCo@C nanohybrid for enhanced electrochemical quantification of nitrofurantoin

Xiaojuan Shui,[a] Huimin Ma,[a] Yuanyuan Zhang,[a,*] Ting Zeng,[a] Juan Yang,[a] Zhen Wu,[b] Xiuhua Zhang,[b] Nianjun Yang[c]

[a]School of Chemistry and Environmental Engineering, School of Materials Science and Engineering, Key Laboratory of Green Chemical Engineering Process of Ministry of Education, Hubei Key Laboratory of Novel Reactor and Green Chemical Technology, Wuhan Institute of Technology, Wuhan 430205, China.
[b]Hubei Collaborative Innovation Center for Advanced Organic Chemical Materials, Ministry of Education Key Laboratory for the Synthesis and Application of Organic Functional Molecules, College of Chemistry and Chemical Engineering, Hubei University, Wuhan, 430062, PR China.
[c]Department of Chemistry & IMO-IMOMEC, Hasselt University Diepenbeek 3590, Belgium.

[*]Corresponding author e-mail: yyzhang@wit.edu.cn (Y. Zhang)

Abstract The development of a high-performance electrochemical sensing platform for monitoring nitrofurantoin (NFT) levels in various real samples plays an important role in the research community worldwide. To accomplish this objective, the crucial challenge is to construct sensing interfaces with outstanding electrocatalytic capabilities. In the present work, a highly efficient metal@carbon electrocatalyst with porous and multi-core-shell nanobox structure comprising polydopamine (PDA)-derived C coated NiCo@C and FeCo@C nanohybrid (named as NiCo@C/FeCo@C@C) was fabricated by simply pyrolyzing NiCo@FeCo prussian blue analogues (PBA)@PDA. The carbonization of PDA into carbon shells protected the framework from collapsing during high-temperature pyrolysis process, thus enlarging the specific surface areas and porosity. The NiCo@C/FeCo@C@C composite attained an enhanced electrochemical capability, such as an outstanding electronic conductivity from the double carbon shell with porous structure, a large

number of active sites and a high electrocatalytic activity from the metallic alloy nanoparticles, which exhibited a highly sensitive response to NFT. Under optimized experimental conditions, the established NiCo@C/FeCo@C@C electrochemical sensor displayed a wide linear range of 0.05-100 μM for NFT determination, coupled with a low detection limit of 14 nM. The practical feasibility of this sensor was also confirmed by the analysis of NFT in tablet and lake water samples with outstanding recovery rates. Moreover, the sustainability of the sensor was demonstrated through its prominent performance in high reproducibility, selectivity and long-term stability. This study thus introduces an innovative approach for the advance of highly efficient electrocatalysts in the area of electrochemical sensing.

Keywords: Electrochemical sensor; Nitrofurantoin; transition metal; Prussian blue analogue; High sensitivity

1. Introduction

Antibiotics are one of the most important medicines that have been intensively and extensively adopted to cure and prevent several diseases as well as acted as growth promoters in domestic animals [1]. Nitrofurantoin (NFT), one of the most commonly used nitrofuran antibiotics, is frequently utilized to treat bladder cancer, hemolytic anemia and acute urinary tract infections (UTIs) [2]. Presently, the standard medicinal amounts of NFT for urinary tract epidemic are 50-200 mg daily. Unfortunately, it has been found that NFT excess can trigger some side effects including dizziness, loss of appetite, nausea, lungs inflammation and liver problems [3]. Additionally, NFT is often found in the environment, which leads to a harmful impact on the ecological system even at very low levels. Consequently, many countries have stringently forbidden the utilization of NFT, nevertheless, it is still unlawfully utilized because of its highly efficient antibacterial properties. In this context, it is very important to exploit an efficient technique that has the capacity to determine NFT quickly, sensitively and accurately in environmental and clinical samples.

To date, different analytical methods have been applied for the quantification of trace NFT, containing fluorescence sensor, surface enhanced Raman scattering, high performance liquid chromatography and electrochemical approaches [4-7]. Among these reported approaches, electrochemical techniques own the advantages of high

sensitivity, ease of monitoring, low price, simple instrumentation and fast response and therefore attract increasing attention toward the determination of NFT [8-11]. Commonly, the materials coated on the working electrode play a critical role for deciding the electrochemical sensing capacity [12-15]. Therefore, searching the highly-efficient electrode materials for NFT determination is greatly desirable.

Various kinds of materials have been exploited as working electrodes for the sensing of NFT, containing metal oxides (e.g., V_2MoO_8 and Sr@Mn_3O_4/GO), Prussian blue analogues (PBA) (e.g., CoCuFe PBA), carbon-based composites (e.g., La_2YBiO_6/multiwalled carbon nanotubes and graphene nanoribbons-MnO_2), MXene-based hybrids (e.g., Pd-$Ti_3C_2T_x$ and Au-polypyrrole-$Ti_3C_2T_x$) and metal-organic frameworks (MOFs) derivatives (e.g., N/Co@CNTs) [16-23].

It is obvious that these sensing materials mainly contain graphene, carbon nanotubes and noble metals, which are expensive. Despite the improved sensitivity for NFT detection on these materials, the high cost, complex handling, and poor durability restrict their wide range of applications. Hence, it is still a challenging task to exploit greatly efficient, cost-effective, and simply accessible sensing materials for NFT electrochemical sensor.

Owing to the cost-effectiveness, abundant reserves, environmentally friendly features, and facile synthesis approaches, transition metals@carbon composites (e.g., Fe, Cu, Ni and Co) have attracted increasing research attention as efficient electrocatalysts to modify electrodes, in which the carbon materials provide excellent electron transport performance and the metal nanoparticles supply high electrocatalytic activity, resulting in good electrochemical detection performance [24-26].

In particular, earlier research has revealed that the Co@C-based catalysts present better catalytic activity and electrochemical sensing performance and have been developed as progressively popular materials in electrochemical sensing platform [27,28]. Nevertheless, pure Co active center exhibits rather mediocre activity and cannot meet the demand for the better sensing performance (e.g., higher sensitivity, wider linear range, etc), hence the catalytic capability and electrochemical sensing performance of these Co@C-based catalysts is urgently to be improved.

Various methods have been announced for boosting the activity of Co@C-based catalysts in the electrochemical detection, among them (i) incorporating Co with other metals to form multi-elemental alloys such as CoFe [29], CoNi [30], CoCu [31], etc.,

yielding various binding sites, acting as active centers and boosting the inherent activity of the catalyst (ii) Altering the structure of the catalysts to fabricate a porous core-shell microstructure to shorten the charge transfer distance and accelerate the mass/charge transfer [32].

Among various fabrication methods for multimetal@carbon materials with core-shell porous structure, high-temperature pyrolysis of Prussian blue analogs (PBAs) has been recognized as an ideal strategy. This is mainly due to the enormous internal surface area, high porosity as well as highly diverse and adjustable structure of the PBAs precursors, in which the ligands transformed to porous graphite carbon matrix with improved electrochemical surface area and high porosities as well as the metal ions converts to metal nanoparticles as new active centers [33,34].

Drawing inspiration from the distinctive properties of trimetallic compounds and porous core-shell architectures, in this work, (i) NiCo PBA nanoboxes were first synthesized as the core employing $K_3[Co(CN)_6]$ as the organic linker and $NiSO_4 \cdot 6H_2O$ as metal nodes. (ii) And then $K_3[Co(CN)_6]$ and $FeSO_4 \cdot 7H_2O$ was added into the solution containing NiCo PBA, obtaining the composite of FeCo PBA shell and NiCo PBA core (i.e., NiCo@FeCo PBA). This process includes coprecipitation and chemical etching processes, in which the solubility product constant (K_{sp}) of $Fe_3[Co(CN)_6]_2$ is smaller than that of $Ni_3[Co\ (CN)_6]_2$ and therefore Fe^{2+} selectively etch the angles of the NiCo PBA core. (iii) NiCo@FeCo PBA was then utilized as nucleation locates for the polymerization of dopamine (DA), resulting in multi-core-shell NiCo@FeCo PBA@polydopamine (PDA) nanoboxes as the precursor. (iv) Finally, NiCo@FeCo PBA@PDA precursor was treated through a high-temperature calcination, in which PDA converted the into a carbon shell with a cubic shape. Meanwhile, the NiCo@FeCo PBA converted into a nanohybrid of carbon coated NiCo alloy (NiCo@C) and carbon coated FeCo alloy (FeCo@C), in which the carbon derived from the organic linker. The final product shows a shape of multi-core-shell nanobox, in which a PDA-derived C cubic shell coating on a hybrid of NiCo@C and FeCo@C, named as NiCo@C/FeCo@C@C (Scheme 1). The carbonization of PDA into carbon shells protected the framework from collapsing during high-temperature pyrolysis process, thus enlarging the specific surface areas and porosity. The obtained NiCo@C/FeCo@C@C composites own distinctive advantages as the sensing materials: (i) firstly, cooperative effects between metal alloy nanoparticles as active centers boost the electrocatalytic activity; (ii) the association of double carbon layers

derived from the ligand and PDA would distinctly enhance the electronic conductivity of the electrocatalyst; (iii) The multi-core-shell nanoboxes with porous structure not only donate to abundant mass transfer tunnels, but also afford more exposed active sites. The results exposed that the established NiCo@C/FeCo@C@C electrochemical sensor displayed the advantages of low detection limit, high reproducibility, long-time stability, high sensitivity and desirable selectivity. Moreover, it also demonstrated the specificity in quantitatively detecting NFT in tablet and lake water samples, thus introducing an innovative approach for the advance of highly efficient electrocatalysts in the area of electrochemical sensing.

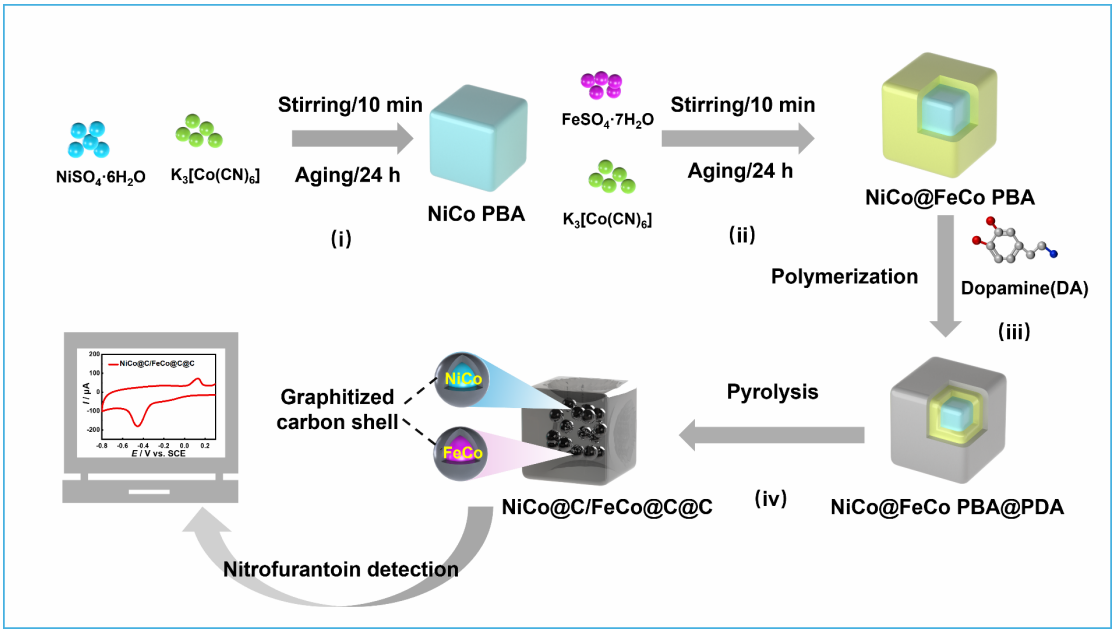

Scheme 1. Schematic to prepare of NiCo@C/FeCo@C@C for the electrochemical determination of NFT.

2. Experimental section

2.1. Reagents

Dopamine hydrochloride ($C_8H_{11}NO_2 \cdot HCl$, analytical grade, 98% purity), disodium hydrogen phosphate dodecahydrate ($Na_2HPO_4 \cdot 12H_2O$, analytical grade, 99% purity), nickel sulfate hexahydrate ($NiSO_4 \cdot 6H_2O$, analytical grade, 98.5% purity), potassium ferricyanide (III) ($K_3[Fe(CN)_6]$, analytical grade, 99.5% purity), trisodium citrate dihydrate ($Na_3C_6H_5O_7 \cdot 2H_2O$, analytical grade, 99% purity), potassium hexacyanocobaltate(III) ($K_3[Co(CN)_6]$, analytical grade, 99% purity), sodium dihydrogen phosphate hydrate ($NaH_2PO_4 \cdot 2H_2O$, analytical grade, 99% purity), iron(II) sulfate heptahydrate ($FeSO_4 \cdot 7H_2O$, analytical grade, 99% purity), N,N-

dimethylformamide (DMF, analytical grade, 99.5% purity), nitrofurantoin (NFT, analytical grade, 98% purity) were procured from Sinopharm Chemical Reagent Company. All the required solutions were prepared utilizing ultrapure water. All reagents used for the measurement of NFT were of analytical quality and utilized as obtained without further purification.

2.2. Synthetic procedure

2.2.1. Syntheses of NiCo PBA and FeCo PBA

6 mmol of $NiSO_4 \cdot 6H_2O$ and 9 mmol of $Na_3C_6H_5O_7 \cdot 2H_2O$ were first dissolved in deionized water (200 mL), which was assigned as solution A. 4 mM $K_3[Co(CN)_6]$ aqueous solution (200 mL) was recorded as solution B. Afterwards, solution B was dropped to solution A, stirred continuously for 10 min and then aged for 24 h at room temperature. The powdery product of NiCo PBA precursor was harvested by a centrifuge, washed with deionized water and ethanol several times, and dried in a vacuum oven overnight at 60 °C. For comparison, FeCo PBA was produced by means of the same method using 6 mmol $FeSO_4 \cdot 7H_2O$ instead of 6 mmol of $NiSO_4 \cdot 6H_2O$.

2.2.2. Syntheses of NiCo@FeCo PBA

NiCo@FeCo PBA were prepared based on the previous reported procedures [35]. 6 mmol of $FeSO_4 \cdot 7H_2O$ and 9 mmol of $Na_3C_6H_5O_7 \cdot 2H_2O$ were added in 200 mL deionized water to form solution A, and then 1 g of the above prepared NiCo PBA was added into solution A. 4 mmol of $K_3[Co(CN)_6]$ was dissolved with 200 mL of deionized water to obtain solution B. Then, solution B was dropped to solution A under vigorous stirring conditions, stirred continuously for 10 min and then aged at room temperature for 24 h. The formed precipitate of NiCo@FeCo PBA precursor was centrifuged, washed with deionized water, and dried in a vacuum oven overnight at 60 °C.

2.2.3. Syntheses of NiCo@FeCo PBA@PDA

NiCo@FeCo PBA@PDA were prepared based on the previous reported procedures with a small change [36].160 mg of the above prepared NiCo@FeCo PBA materials were dispersed in 200 mL of tris-buffer solution (10 mM, pH 8.5), and then the obtained dispersion was ultrasonicated for 0.5 h, followed by the addition of 160 mg of dopamine hydrochloride with continuous stirring at room temperature for 4 h. The product was collected by centrifugation, washed with DI water and ethanol for multiple times, and followed by vacuum drying for 12 h at 60 °C.

2.2.4. Syntheses of NiCo@C/FeCo@C and NiCo@C/FeCo@C@C

The obtained precursors including NiCo@FeCo PBA and NiCo@FeCo PBA@PDA were pyrolyzed at 600 for 2 h with a heating rate of 2 min^{-1} under N_2 atmosphere, and the NiCo@C/FeCo@C and NiCo@C/FeCo@C@C were gained, respectively [37]. By means of the same process, NiCo@C and FeCo@C were produced through replacing the precursor with NiCo PBA and FeCo PBA, respectively.

2.3. Fabrication of the NiCo@C/FeCo@C@C sensor

A glassy carbon electrode (GCE, d = 3 mm) was smoothed with alumina suspension to a mirror finish, washed successively with ethanol and deionized water, and dried naturally. In the meantime, the as-prepared NiCo@C/FeCo@C@C was dispersed into DMF and sonicated for 20 min to improve the homogeneity, forming the uniform NiCo@C/FeCo@C@C dispersion with the concentration of 2 mg mL^{-1}. Then, a certain quantity of NiCo@C/FeCo@C@C dispersion liquid was drop-casted on the cleaned electrode surface, and then drying it under an infrared lamp, gaining a NiCo@C/FeCo@C@C modified GCE. The same method was employed to prepare GCEs modified with the precursors including NiCo@FeCo PBA@PDA, NiCo@FeCo PBA, FeCo PBA, NiCo PBA, and the derived materials including NiCo@C, FeCo@C, NiCo@C/FeCo@C.

2.4. Instruments

The morphology and size of the electrocatalysts were observed with a JEOL-JSM-7100F scanning electron microscope (SEM) and a Tecnai G2 20 S-TWIN transmission electron microscope (TEM). Raman spectrum was accomplished utilizing a DXR Raman spectrometer (Thermo Fisher Scientific, Waltham, Massachusetts) with a 532 nm diode laser. Powder X-ray diffraction (XRD) experiments were carried out on a D8 ADVANCE (BRUKER, Germany) diffractometer. The Brunauer-Emmett-Teller (BET) surface area and pore size distribution were measured on a Micromeritics ASAP 2020 at 77 K. X-ray photoelectron spectroscopy (XPS) data were attained an X-ray photoemission spectrometer (AXIS Ultra DLD). A CHI660E electrochemical workstation was adopted to conduct the electrochemical experiments and analyses were studied. The prepared materials coated glassy carbon electrode (GCE) was directly utilized as the

working electrode. The auxiliary electrode was a Pt wire and the reference electrode was a saturated calomel electrode (SCE, saturated KCl). For the analysis of a real sample, high-pressure liquid chromatography (HPLC Agilent 1100) with ProntosIl KromaPlus C18 column (150 × 4.6 mm, 5 μm, Bischoff Chromatography, Germany) and a UV detector was performed at an operational wavelength of 365 nm.

2.5. Preparation of the real sample

The practical probability of proposed NiCo@C/FeCo@C@C sensor for the voltammetric analysis of NFT in the environmental samples of local lake water (Wuhan, China) and drug samples (e.g., NFT-containing tablets) was studied. The lake water samples were filtered through a 0.22 μm membrane and then further diluted with 0.2 M pH 7.0 PBS at a volume ratio of 1:1 for the following electrochemical analysis. NFT-containing tablets used in this work were bought from the local medical store. The tablets were precisely weighed, totally grounded and dissolved in DMF. Then 50 μL of the treated sample solutions was added to the electrochemical cells containing 10 mL 0.1 M PBS buffer (pH 7.0).

3. Results and discussion

3.1. Structural and Chemical Analysis

The morphology and structure of the precursors including NiCo PBA, FeCo PBA NiCo@FeCo PBA and NiCo@FeCo PBA@PDA as well as the corresponding derivatives including NiCo@C, FeCo@C, NiCo@C/FeCo@C and NiCo@C/FeCo@C@C were characterized by SEM and TEM. Fig. 1A and 1B are the SEM and TEM images of NiCo PBA, and it can be seen that NiCo PBA displays a highly regular cubic morphology with average lateral size of approximately 200 nm. Fig. 1C and 1D present that the FeCo PBA precursor also possesses monodisperse cubes. The SEM analysis of the obtained NiCo@FeCo PBA compostie shows that this composite also displays a monodisperse nanocube morphology with a smooth surface (Fig. 1E). The core-shell structure of NiCo@FeCo PBA with the cube edge length of ~250 nm and the 30 nm-thick shell is demonstrated by its TEM image (Fig. 1F). After coating NiCo@FeCo PBA by PDA, the cubic morphology of NiCo@FeCo PBA@PDA basically remains (Fig. 1G), and the TEM image demonstrates that the NiCo@FeCo PBA was covered with a very thin and smooth PDA layer (Fig. 1H). The elemental mapping analysis of NiCo@FeCo PBA (Fig. 1I) illustrates the

distribution of C, N, Co, Ni and Fe elements in NiCo@FeCo PBA. Moreover, it can be noticed that Ni elements are mostly dispersed in the part of core, while Fe elements are mostly allocated in the part of shell and Co elements are distributed in the entire cube, confirming core-shell structure of the NiCo@FeCo PBA, which is consistent with the experimental result reported in literature [35].

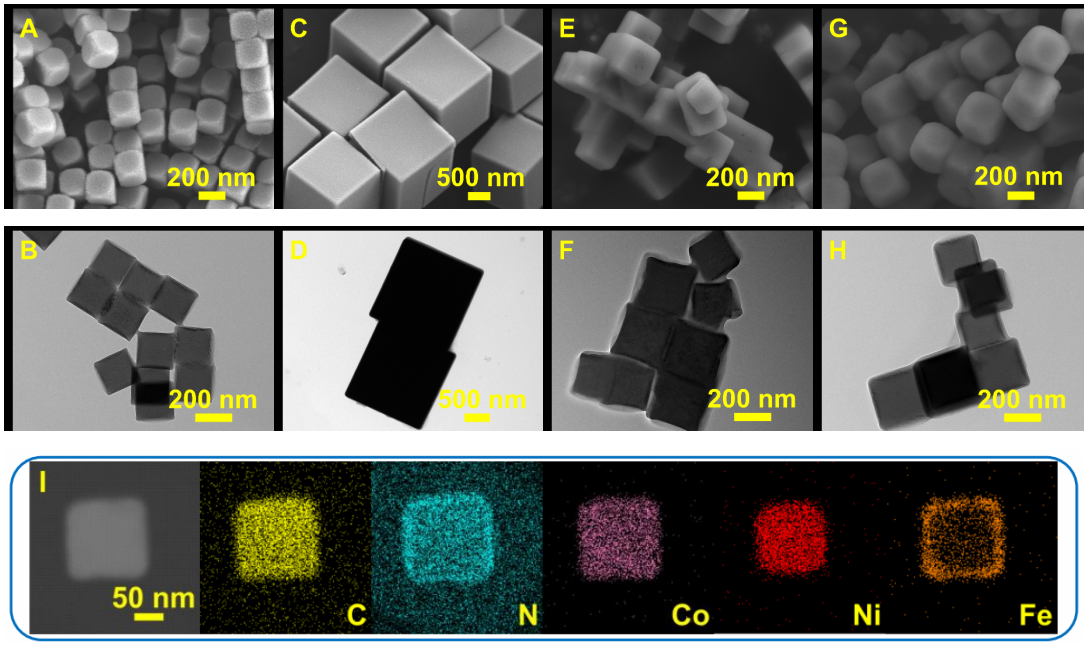

Fig. 1. SEM and TEM images of NiCo PBA (A,B), FeCo PBA (C,D) NiCo@FeCo PBA (E,F) and NiCo@FeCo PBA@PDA (G,H). Elemental mapping images of NiCo@FeCo PBA (I).

Fig. 2 shows the morphology and structure of the corresponding derivatives including NiCo@C, FeCo@C, NiCo@C/FeCo@C and NiCo@C/FeCo@C@C obtained by carbonization at a high temperature, examined by SEM and TEM. After calcination and annealing, the product of NiCo PBA precursor cannot maintain the cubic morphology, however it collapsed and transformed into bulk particles with irregular morphology with a size of about 280 nm (Fig. 2A). The TEM image (Fig. 2B) clearly displays that the obtained composites have a core-shell structure, with the state of carbon layer coating NiCo alloy (named as NiCo@C). Similarly, the FeCo PBA cube was also completely destroyed during heat treatment, leading to the formation of numerous disordered core-shell nanoparticles with the average size of ~80 nm, in which the core is FeCo alloy and the shell is a carbon layer (named as FeCo@C) (Fig. 2C and 2D). As for the obtained samples derived from the cubic NiCo@FeCo PBA precursor without the PDA coating, the cubic morphology

disappeared and transformed into irregular nanoparticles with the size range of 30 to 80 nm, and these nanoparticles tend to aggregate (Fig. 2E). As presented in Fig. 2F and 2G, these nanoparticles display core-shell structure, in which the alloy nanoparticels (i.e., NiCo alloy and FeCo alloy) wrapped within the carbon shell with thickness of ~15 nm (denoted as NiCo@C/FeCo@C). In Fig. 2H, the HRTEM images of these core-shell structures display lattice fringes with interplane distances of 0.330 nm, corresponded to (002) plane of graphitic carbon in the shell. In addition, in the core portion of two random particles, two kinds of interplanar spacing distance of 0.210 nm and 0.201 nm were observed, which is in accord with the (111) plane of NiCo and (110) plane of FeCo, respectively. These HRTEM results demonstrated the formation of NiCo@C/FeCo@C composite after a pyrolysis treatment of NiCo@FeCo PBA precursor. However, after calcination of NiCo@FeCo PBA@PDA, the product can maintain the cubic morphology of precursor with a side length of approximately 200 nm, only the cube surface displayed a slight concavity, demonstrating that the PDA coating is helpful to maintain the morphology of the templates under high-temperature treatment (Fig. 2I). The derived products of NiCo@FeCo PBA@PDA were explored by TEM (Fig. 2J and 2K), and it can be clearly obtained that the products exhibit a core-shell cube structure with many nanoparticles enveloped in a 30 nm-thick shell. The amorphous carbon shell is produced from the carbonization of PDA at a high temperature. Moreover, HRTEM (Fig. 2L) is utilized to characterize the nanoparticles in the core of the cube, and these nanoparticles also show a core-shell structure. The image reveals the fringe spacing of 0.210 nm, 0.200 nm and 0.330 nm for (111), (110) and (002) lattice planes of NiCo alloy, FeCo alloy and graphitic carbon, respectively. These results propose that the surface of the NiCo alloy and FeCo alloy is respectively coated with a graphitic carbon shell, forming a NiCo@C/FeCo@C composite. Then, many NiCo@C/FeCo@C core-shell particles, as the core, wrapped with PDA-transformed amorphous carbon shell, forming multi-core-shell structure (denoted as NiCo@C/FeCo@C@C nanoboxes). Additionally, the corresponding EDS mapping of NiCo@C/FeCo@C@C nanoboxes in Fig. 2M exposes that C, N, Co, Fe, and Ni elements are uniformly distributed. The porous and multi-core-shell structure provide a huge interfacial contact area and more exposed active sites that promote the transfer of electrons, thereby ensuring prominent sensing capability of NiCo@C/FeCo@C@C nanoboxes.

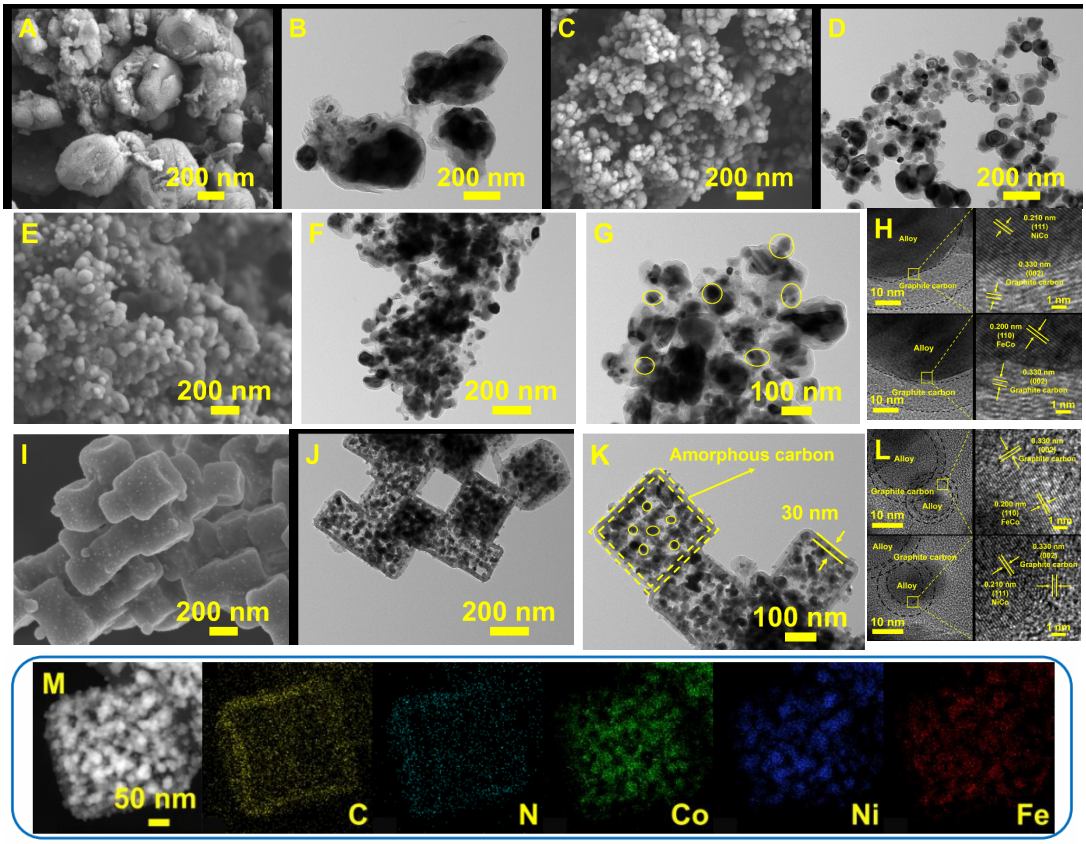

Fig. 2. SEM and TEM images of NiCo@C (A,B), FeCo@C (C,D), NiCo@C/FeCo@C (E,F,G) and NiCo@C/FeCo@C@C (I,J,K); HRTEM images of NiCo@C/FeCo@C (H) and NiCo@C/FeCo@C@C (L). Elemental mapping images of NiCo@C/FeCo@C@C (M).

The crystal structures of the four precursors (i.e., NiCo PBA, FeCo PBA NiCo@FeCo PBA and NiCo@FeCo PBA@PDA) and the corresponding derivatives (i.e., NiCo@C, FeCo@C, NiCo@C/FeCo@C and NiCo@C/FeCo@C@C) were verified by means of X-ray diffraction (XRD) test. In the XRD patterns of NiCo PBA (Fig. 3A-a) and FeCo PBA (Fig. 3A-b), the typical diffraction peaks appear at around 17.4° or 17.1°, 24.7° or 24.3° and 35.3° or 34.7°, ascribed to (200), (220) and (400) planes of $Ni_3[Co(CN)_6]_2$ PBA phase (JCPDS: 89-3738) and $Fe_3[Co(CN)_6]_2$ PBA phase (JCPDS: 46-0907), respectively, demonstrating the effective preparation of NiCo PBA and FeCo PBA. In addition, the characteristic diffraction peaks of NiCo@FeCo PBA (Fig. 3A-c) and NiCo@FeCo PBA@PDA (Fig. 3A-d) are consistent with the patterns of NiCo PBA and FeCo PBA, indicating the core-shell structures were successfully prepared.

Fig. 3B displays the XRD characteristic patterns of the corresponding derivatives

(i.e., NiCo@C, FeCo@C, NiCo@C/FeCo@C and NiCo@C/FeCo@C@C). The XRD plots of NiCo@C possess intense peaks centered at 44.4°, 51.7°, and 76.2°, which lie between Co (JCPDS: 15-0806) and Ni (JCPDS: 04-0850), which can be indexed to (111), (200), and (220) planes of the NiCo alloy, respectively (Fig. 3B-a). Additionally, the intense peaks located at 44.8°, 65.2°, 82.6° belong to the FeCo@C sample (Fig. 3B-b), matching well with the (110), (200) and (211) plane of FeCo alloy (JCPDS: 49-1568). As for the NiCo@C/FeCo@C (Fig. 3B-c) and NiCo@C/FeCo@C@C (Fig. 3B-d), the XRD patterns possess the characteristic peaks of located at 44.0° or 44.4°, 44.8° or 44.9°, 51.3° or 51.7°, 65.2° or 65.3°, 75.5° or 76.1°, 82.6 or 82.7 belong to the NiCo alloy and FeCo alloy, demonstrating the effective construction of NiCo alloy and FeCo alloy in these composites. For further examination of crystal structure, Rietveld refinement was conducted for the corresponding derivatives (i.e., NiCo@C, FeCo@C, NiCo@C/FeCo@C and NiCo@C/FeCo@C@C) by means of General Structure Analysis System, as displayed in Fig. 3C-3F. The results are well consistent with experimental and calculated intensity patterns, confirming the superior quality of prepared materials. The XRD results specify that NiCo alloy and FeCo alloy are successfully generated from NiCo@FeCo PBA@PDA after pyrolysis, indicating the construction of NiCo@C/FeCo@C and NiCo@C/FeCo@C@C.

X-ray photoelectron spectroscopy (XPS) was carried out to investigate the detailed elemental composition and oxidation states of the NiCo@C/FeCo@C and NiCo@C/FeCo@C@C. Fig. 4A offers the survey spectra of NiCo@C/FeCo@C and NiCo@C/FeCo@C@C, which verify the presence of N, Co, Ni and Fe elements in these materials. Figure 4B, 4C and 4D display that all the high-resolution Fe 2p spectrum, Ni 2p spectrum and Co 2p spectrum have two spin-orbit doublets ($2p_{1/2}$ and $2p_{3/2}$) and two shakeup satellite peaks (marked by sat.). The Fe $2p_{3/2}$ (~707.4 eV for Fe^0, ~710.5 eV for Fe^{2+} and ~712.8 eV for Fe^{3+}) and Fe $2p_{1/2}$ (~718.3 eV for Fe^0, ~721.1 eV for Fe^{2+} and ~723.7 eV for Fe^{3+}) peaks can be observed in the high-resolution Fe 2p spectra (Fig. 4B). Three kinds of Ni species can be surveyed with the peaks at 853.1 eV and 870.4 eV indexed to Ni^0, the peaks at 854.2 eV and 872.1 eV assigned to Ni^{2+}, and the peaks at 855.7 eV and 873.8 eV corresponding to Ni^{3+} (Fig. 4C) .A couple of peaks located at about 778.5 and 794.0 eV are associated with Co^0, and the second couple of peaks appeared at about 780.1 and 797.3 eV are

corresponding to Co^{3+}, and another couple of peaks at around 782.3 and 799.0 eV are attributed to Co^{2+} (Fig. 4D). Accordingly, various alloyed nanoparticles are formed in the NiCo@C/FeCo@C and NiCo@C/FeCo@C@C. The metal centers in these alloyed nanoparticles are thus active sites and are beneficial to gain outstanding electrochemical catalytic performance.

The structural defects and graphitization degree of two derivatives (i.e., NiCo@C/FeCo@C and NiCo@C/FeCo@C@C) were analyzed by Raman technique. Two distinct peaks at 1351 cm^{-1} and 1591 cm^{-1} in the Raman spectrum (Fig. 4E) can be attributed to D band and G band features of carbon-based materials. The band intensity ratio between the D and G bands (I_D/I_G) is normally exploited to evaluate the degree of carbon graphitization. The values (I_D/I_G) of are calculated to be 1.32 and 1.18 for NiCo@C/FeCo@C and NiCo@C/FeCo@C@C, respectively, indicating a higher degree of graphitization in NiCo@C/FeCo@C@C, which can generate higher electron transfer ability to improve sensing capability.

The nitrogen adsorption-desorption analysis (Fig. 4F) shows that NiCo@C/FeCo@C@C owns a Brunauer-Emmett-Teller (BET) specific surface area of 110.61 $m^2\ g^{-1}$ and a pore volume of 0.368 $cm^3\ g^{-1}$, which are nearly 4 times those of NiCo@C/FeCo@C (25.64 $m^2\ g^{-1}$ and 0.077 $cm^3\ g^{-1}$, respectively). Additionally, an average pore diameter of 12.0 nm and 10.0 nm were observed for NiCo@C/FeCo@C@C and NiCo@C/FeCo@C, respectively (Fig. 4G). It can be concluded that the construction of carbon nanoboxes with hierarchical multi-core-shell structure increases the BET surface area and pore volume of NiCo@C/FeCo@C@C, which can offer NiCo@C/FeCo@C@C more excellent mass transfer channel, reduce the mass transport resistance and boost the electrochemical sensing capability.

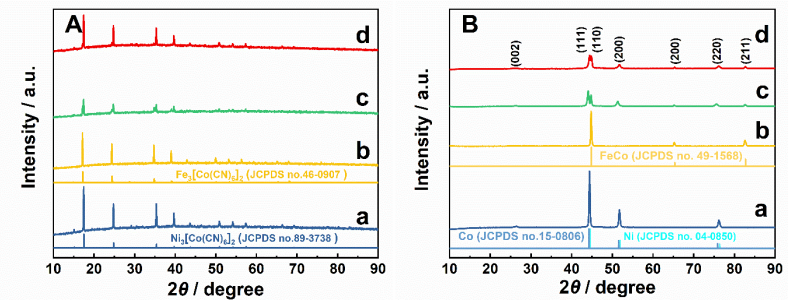

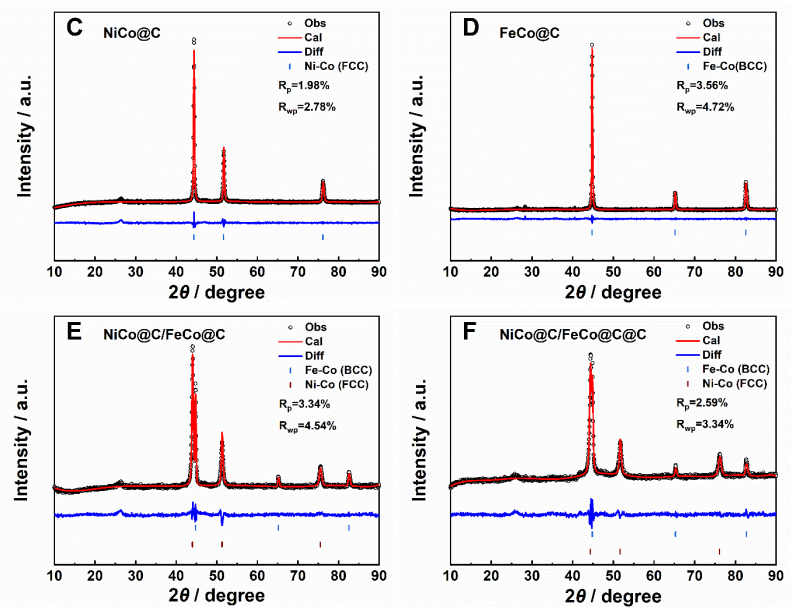

Fig. 3. (A) XRD patterns of NiCo PBA (a), FeCo PBA (b), NiCo@FeCo PBA (c) and NiCo@FeCo PBA@PDA (d); (B) XRD patterns of NiCo@C (a), FeCo@C (b), NiCo@C/FeCo@C (c) and NiCo@C/FeCo@C@C (d); (C-F) Rietveld refinement patterns of NiCo@C (C), FeCo@C (D), NiCo@C/FeCo@C (E) and NiCo@C/FeCo@C@C (F).

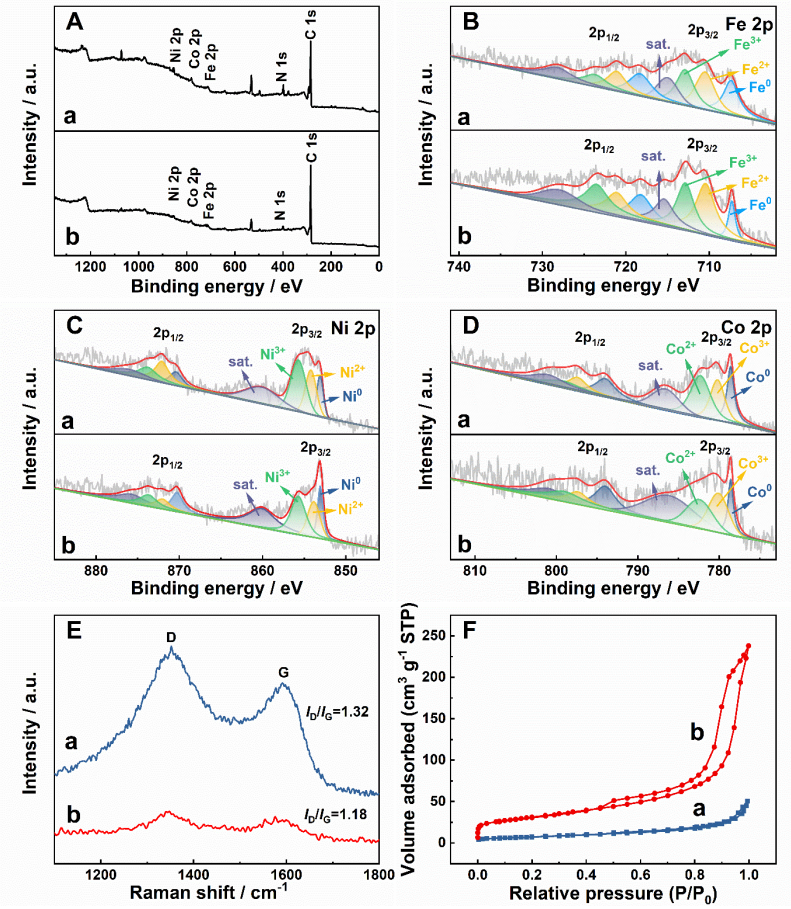

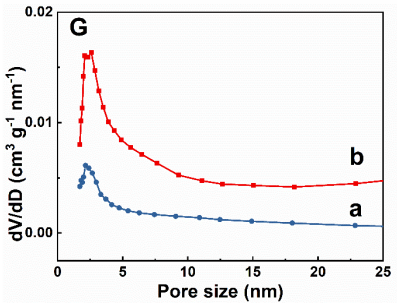

Fig. 4. (A) XPS survey spectrum of NiCo@C/FeCo@C (a) and NiCo@C/FeCo@C@C (b); High-resolution XPS spectrum of Fe 2p (B), Ni 2p (C) and Co 2p (D) for the NiCo@C/FeCo@C (a) and NiCo@C/FeCo@C@C (b). (E) Raman Spectrum of NiCo@C/FeCo@C (a) and NiCo@C/FeCo@C@C (b). N_2 absorption/desorption isotherms (F) and BJH pore size distribution (G) of NiCo@C/FeCo@C (a) and NiCo@C/FeCo@C@C (b).

3.2. Electrochemical properties of different modified electrodes

These composites (e.g., the precursors including NiCo@FeCo PBA@PDA, NiCo@FeCo PBA, FeCo PBA, NiCo PBA, and the derived materials including NiCo@C, FeCo@C, NiCo@C/FeCo@C, NiCo@C/FeCo@C@C) were covered on the bare electrode and their electrochemical performances were investigated using cyclic voltammetry (CV) and electrochemical impedance spectroscopy (EIS) experiments. In the first step, CV curves were recorded for 5 mM $[Fe(CN)_6]^{3-/4-}$ in 0.1 M KCl on these electrode surface (Fig. 5A and 5B). On these working electrodes, a couple of noticeable quasi-reversible redox peaks are detected in their CV curves. As exhibited in Fig. 5A, compared to the anodic peak current (I_{pa}) of bare GCE (96.22 μA), lower I_{pa} values were observed on the GCE modified with NiCo@FeCo PBA@PDA (80.37 μA), NiCo@FeCo PBA (79.97 μA), FeCo PBA (72.02 μA) and NiCo PBA (70.46 μA), proving that the poor conductivity of these precursors is unfavorable for the charge transferring process. As showed in Fig. 5B, compared to the above electrodes, higher I_{pa} values were observed on the GCE modified with NiCo@C (101.0 μA) and FeCo@C (104.9 μA), proving that NiCo@C and FeCo@C effectively enhanced the conductivity and boosted the charge transferability. After the modification of NiCo@C/FeCo@C on the GCE surface, the I_{pa} value further increased to 113.5 μA, owing to the good electron transfer properties resulting from the cooperative effect of multiple metallic alloy centers existing in the NiCo@C/FeCo@C composite. Obviously, the highest I_{pa} value (140.6 μA) was gained at the

NiCo@C/FeCo@C@C modified GCE, proving the most outstanding electron-transfer ability and the largest electrochemical active areas. This is probably due to the porous structure, higher surface area and the double carbon shell of the NiCo@C/FeCo@C@C multi-core-shell nanoboxes, which can improve the mass transfer efficiency.

EIS is an effective method to explore the characteristics (e.g., electron charge transfer kinetics) of these electrode interfaces. Fig. 5C and 5D showed the recorded Nyquist plots of these working electrodes in 0.1 M KCl containing 5 mM $[Fe(CN)_6]^{3-/4-}$. To evaluate the surface variations, charge transfer resistance (R_{ct}) was selected for comparing on different modified GCEs. Based on the Randles circuit in the inset of Fig. 5C and 5D, these Nyquist plots was fitted and the model consists of the double-layer capacitance (C_{dl}) between the working electrode and electrolytic solution, the electrolyte resistance (R_s), Warburg impedance (Z_w) and electron-transfer resistance (R_{ct}), of which the values are presented in Table 1. The R_{ct} value at the GCE modified with NiCo@FeCo PBA@PDA, NiCo@FeCo PBA, FeCo PBA, NiCo PBA and the bare GCE is 299.7 Ω, 350.3 Ω, 493.5 Ω, 577.9 Ω and 112.8 Ω, respectively, indicating the slow electron transport on these electrodes (Fig. 5C). The R_{ct} value for GCE modified with NiCo@C and FeCo@C declined to 55.37 Ω and 49.97 Ω, respectively, signifying that the electrochemical reaction and charge transfer were enhanced at the NiCo@C and FeCo@C modified GCE surface. Furthermore, the modification of the NiCo@C/FeCo@C on the GCE surface decreases the R_{ct} value to 29.01 Ω demonstrating the fast electron transfer rate between the electrode surface and electrolyte interfaces. After further modification, NiCo@C/FeCo@C@C modified GCE owns the smallest R_{ct} value to 18.43 Ω (Fig. 5D), indicating superior electron transfer capability. This is mainly due to the unique structure of the porous multi-core-shell nanoboxes, which can supply easy electron transport pathway between the electrode and the electrolyte. The NiCo@C/FeCo@C@C composite presents greater catalytic activity and reflects its potential for electrochemical detection of NFT in solutions.

The electrochemical behavior of NFT on a GCE as well as GCEs modified with the precursors including NiCo@FeCo PBA@PDA, NiCo@FeCo PBA, FeCo PBA, NiCo PBA, and the derived materials including NiCo@C, FeCo@C, NiCo@C/FeCo@C, NiCo@C/FeCo@C@C was studied by CV technique in PBS (0.1 M, pH 7.0) (Fig. 5E and 5F). No redox peaks are detected in the CV curves of these

GCEs in the blank solution, namely without NFT (dotted line), while the cathodic peaks are recorded in the solution containing NFT (solid line). Note that on the bare electrode only a pretty small reduction peak (3.11 μA) at a potential of -0.477 V is observed for NFT. The reduction of NFT displays a slightly higher current and more anodic potential employing NiCo@FeCo PBA@PDA (9.45 μA, -0.462 V), NiCo@FeCo PBA (6.49 μA, -0.455 V), FeCo PBA (5.48 μA, -0.464 V), NiCo PBA (4.62 μA, -0.463 V) modified GCE due to the electrocatalytic active sites in the materials (Fig. 5E). Compared to the above electrodes, NiCo@C and FeCo@C modified GCE displayed stronger electrocatalytic response towards NFT with peak current values of 31.17 μA and 19.24 μA as well as the potential of -0.435 V and -0.404 V, respectively. This is due to the excellent electronic conductivity of the porous carbon shell and the superior electrocatalytic ability of the alloy nanoparticles. Electrocatalytic sensing behavior was further enhanced by coating NiCo@C/FeCo@C on GCE, presenting a peak current value of 37.91 μA, which means that the cooperative effect of NiCo@C and FeCo@C in the NiCo@C/FeCo@C hybrid improves the electrochemical property. Eventually, the highest cathodic peak intensity (53.41 μA) and more anodic potential (-0.405 V) was gained on a NiCo@C/FeCo@C@C modified GCE (Fig. 5F), indicating outstanding electronic conductivity, a large number of active sites and a high electrocatalytic activity of this electrode. The superior sensing performance can be due to the distinctive advantages of the obtained NiCo@C/FeCo@C@C composites as the sensing materials: (i) firstly, cooperative effects between metal alloy nanoparticles as active centers boost the electrocatalytic activity; (ii) the association of double carbon layers derived from the ligand and PDA would distinctly enhance the electronic conductivity of the electrocatalyst; (iii) The multi-core-shell nanoboxes with porous structure not only donate to abundant mass transfer tunnels, but also afford more exposed active sites.

It is obvious that NiCo@C/FeCo@C and NiCo@C/FeCo@C@C modified GCEs displayed excellent sensing performance for NFT, hence, to further explore and compare the electrochemical kinetic information of these electrodes, the standard heterogeneous charge-transfer rate constant (k^o) was extracted utilizing the rotating disk electrode (RDE) voltammetry technique. The RDE voltammetric profiles recorded using varying electrode rotation speed (ω) in 1 M KCl containing 5 mM $Ru(NH_3)_6Cl_3$ for different electrodes are provided in Fig. 6A-6C. The k^o values were assessed on the basis of the Koutecky-Levich equation [11], they are 0.095, 0.109 and

0.395 cm s^{-1} for a GCE, a NiCo@C/FeCo@C modified GCE and a NiCo@C/FeCo@C@C modified GCE, respectively (Fig. 6D). The highest k^o value obtained for NiCo@C/FeCo@C@C modified GCE proposed improved charge transfer rate and increased conductivity for electrochemical sensing of NFT (Fig. 6H).

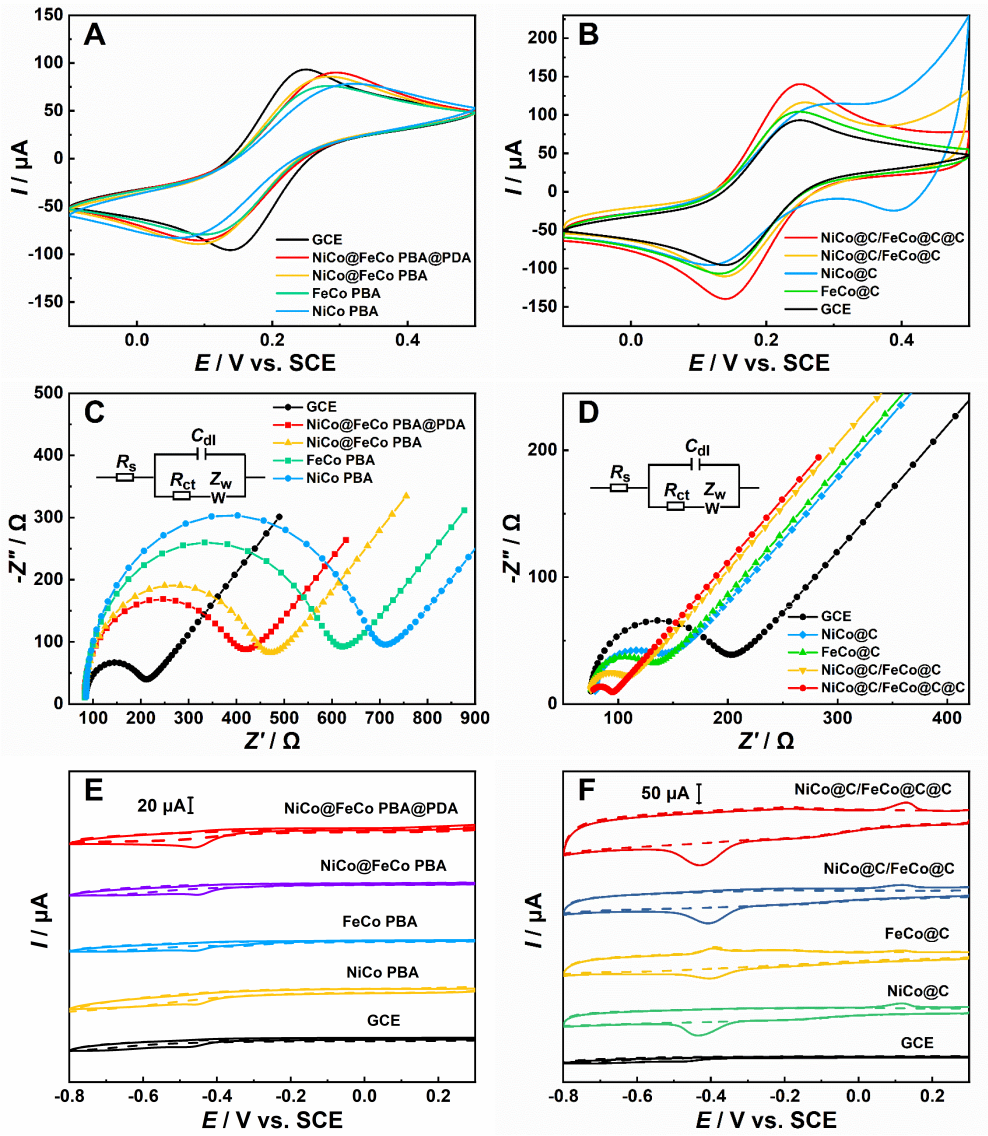

Fig. 5. (A,B) CV responses and (C,D) EIS spectra of a GCE, as well as a GCE modified with the precursors including NiCo@FeCo PBA@PDA, NiCo@FeCo PBA, FeCo PBA, NiCo PBA, and the derived materials including NiCo@C, FeCo@C, NiCo@C/FeCo@C and NiCo@C/FeCo@C@C in 0.1 M KCl containing an equimolar (5 mM) mixture of $K_3Fe(CN)_6$ and $K_4Fe(CN)_6$. The Inset in (C and D) is the Randles equivalent circuit model. EIS test is at open circuit potentials (E,F). CV curves of a GCE, as well as a GCE modified with the precursors including NiCo@FeCo PBA@PDA, NiCo@FeCo PBA, FeCo PBA, NiCo PBA, and the derived materials including NiCo@C, FeCo@C, NiCo@C/FeCo@C and

NiCo@C/FeCo@C@C without (dashed line) and with (solid line) 100 μM NFT.

Table 1. The electrochemical impedance data of various electrodes in 5 mM $[Fe(CN)_6]^{3-/4-}$ + 0.1 M KCl.

Electrode	R_s (Ω)	C_{dl} (F)	R_{ct} (Ω)	Z_w (Ω $s^{-1/2}$)
NiCo PBA	256.3	0.527×10^{-6}	577.9	0.0010
FeCo PBA	109.8	0.452×10^{-6}	493.5	0.0008
NiCo@FeCo PBA	97.2	0.464×10^{-6}	350.3	0.0007
NiCo@FeCo PBA@PDA	134.6	1.208×10^{-6}	299.7	0.0010
GCE	112.1	0.475×10^{-6}	112.8	0.0008
NiCo@C	136.1	1.755×10^{-6}	55.37	0.0009
FeCo@C	195.4	0.594×10^{-6}	49.97	0.0007
NiCo@C/FeCo@C	109.9	0.620×10^{-6}	29.01	0.0009
NiCo@C/FeCo@C@C	81.39	0.204×10^{-6}	18.43	0.0013

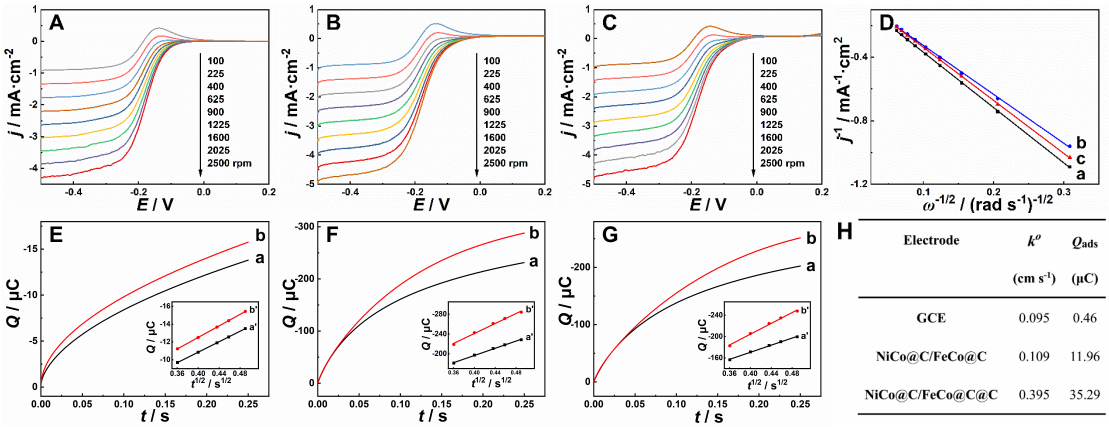

Fig. 6. RDE voltammetric profiles recorded in 1 M KCl and 5 mM $Ru(NH_3)_6Cl_3$ on a GCE (A), a NiCo@C/FeCo@C modified GCE (B), and a NiCo@C/FeCo@C@C modified GCE (C) using varying electrode rotation speed; (D) Corresponding Kouteckye-Levich plots on a GCE (a), a NiCo@C/FeCo@C modified GCE (b), and a NiCo@C/FeCo@C@C modified GCE (c). (E-G) Chronoamperograms (a and b) and linear fitting graph of Q *vs.* $t^{1/2}$ (a' and b') in PBS (0.1 M) supporting electrolyte (pH = 7.0) in the absence (a and a') or presence of 10 μM NFT (b and b') on a GCE (E), a NiCo@C/FeCo@C modified GCE (F), and a NiCo@C/FeCo@C@C modified GCE (G). (H) The responding values of k^o and Q_{ads}.

Moreover, the adsorption phenomenon of NFT on these electrodes was investigated by chronocoulometry (CC), and the related charge (Q)-time (t) curves were recorded on a GCE (Fig. 6E), a NiCo@C/FeCo@C modified GCE (Fig. 6F) and a NiCo@C/FeCo@C@C (Fig. 6G) modified GCE. As displayed in Fig. 6E, while the GCE working electrode was put into a 0.1 M pH 7.0 PBS solution with the analytes for test, gaining the Q-t curve (Fig. 6E-a). As displayed in the insets in Fig. 6E, the relationship linear plots of Q-$t^{1/2}$ could be gained through extracting data from Q-t curves (Fig. 6E-a′). Then, the CC test was carried out in an electrolyte solution containing 10 μM NFT, and the Q-t curve (Fig. 6E-b) under the same test condition was recorded with a Q-$t^{1/2}$ straight line (Fig. 6E-b′). According to Anson's theory, Q_{ads} denotes the Faradaic charge caused by the reduction of the adsorbed NFT, and the Q_{ads} value is the equivalent of the intercept difference between curve b′ and curve a′. Accordingly, the Q_{ads} values for NFT on a GCE, a NiCo@C/FeCo@C modified GCE and a NiCo@C/FeCo@C@C modified GCE were acquired as 0.46 μC, 11.96 μC and 35.29 μC, respectively (Fig. 6H). The results proposed that NiCo@C/FeCo@C@C possesses a superior adsorption capability of NFT, which is mainly due to its unique structure of porous multi-core-shell nanoboxes, which can significantly expand its electrode effective surface area and capability of NFT adsorption sites.

3.3. Electrochemical sensing applications

In order to optimize the buffer solution's pH for the quantification of NFT on NiCo@C/FeCo@C@C modified GCE, the CV curves of 100 μM NFT in PBS (0.1 M) with different pH values (from 6.0 to 8.0) on the above electrode were displayed in Fig. 7A. It is obvious that as pH increases from pH 6.0 to 7.0, the cathodic peak current (I_{pc}) of NFT gradually increased (the inset I of Fig. 7A). The I_{pc} achieved the maximum value in the supporting electrolyte with a pH value of 7.0, and then diminish as pH increased between pH 7.0 and 8.0. Consequently, in the subsequent tests, a pH 7.0 PBS (0.1 M) was adopted as the supporting solution. Moreover, the cathodic peak potentials (E_{pc}) of NFT continuously shift to more cathodic ones with the growing of pH value, representing the participation of protons in the electrochemical reaction of NFT. The E_{pc} values had good linearity with the pH values of the supporting electrolyte, and the equation can be acquired as E_{pc} (V) = -0.045 - 0.060 pH (R^2 = 0.996) (the inset II of Fig. 7A). The absolute value of the slope was close to the theoretical value attained from the Nernst equation (-59 mV pH^{-1}),

demonstrating that an equal number of transferred electrons and protons were engaged in the NFT reduction process on the NiCo@C/FeCo@C@C modified GCE, as shown in Scheme 2.

CV curves for NiCo@C/FeCo@C@C modified GCE at various scan rates (v, from 40 to 200 mV s^{-1}) were recorded in a 100 μM NFT solution to explore the electrode reaction behavior of NFT based on the relationship of I_{pc} and E_{pc} with v (Fig. 7B). As increasing v, the I_{pc} values of NFT raised linearly as v increased, demonstrating that the electrochemical reaction of NFT on the NiCo@C/FeCo@C@C modified GCE surface was an adsorption-controlled process (the inset I of Fig. 7B). Meanwhile, with the growth of v, the cathodic peak of NFT negatively shifted. The E_{pc} and ln v were linearly fitted (the inset II of Fig. 7B). The obtained linear regression equation was E_{pc} (V) = 0.045 ln v - 0.241 (R^2 = 0.999).

To gain a proper performance of the constructed sensor, the influences including the suspension amounts of NiCo@C/FeCo@C@C materials and accumulation time were assessed. Fig. 7C displays the cathodic peak current values for GCE modified with different amounts of NiCo@C/FeCo@C@C. It was apparent that GCE modified with 3 μL of NiCo@C/FeCo@C@C gains the largest electrochemical signal and hence 3 μL was optimal for NFT detection. Meanwhile, the electrochemical signal is notably affected by the accumulation time, the influence of cumulative time on cathodic peak current was further evaluated. The results showed that as the accumulation time was varied from 2 min to 5 min, a progressive enhance in the peak response of NFT was observed. Nevertheless, further lengthening of the accumulation time did not cause large variations in the peak response (Fig. 7D). These results propose that the optimal accumulation time is 5 min for attaining the largest peak current in NFT determination utilizing NiCo@C/FeCo@C@C.

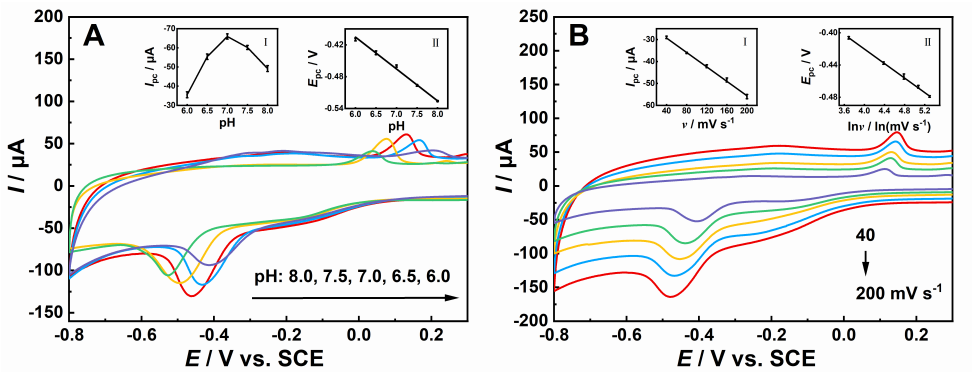

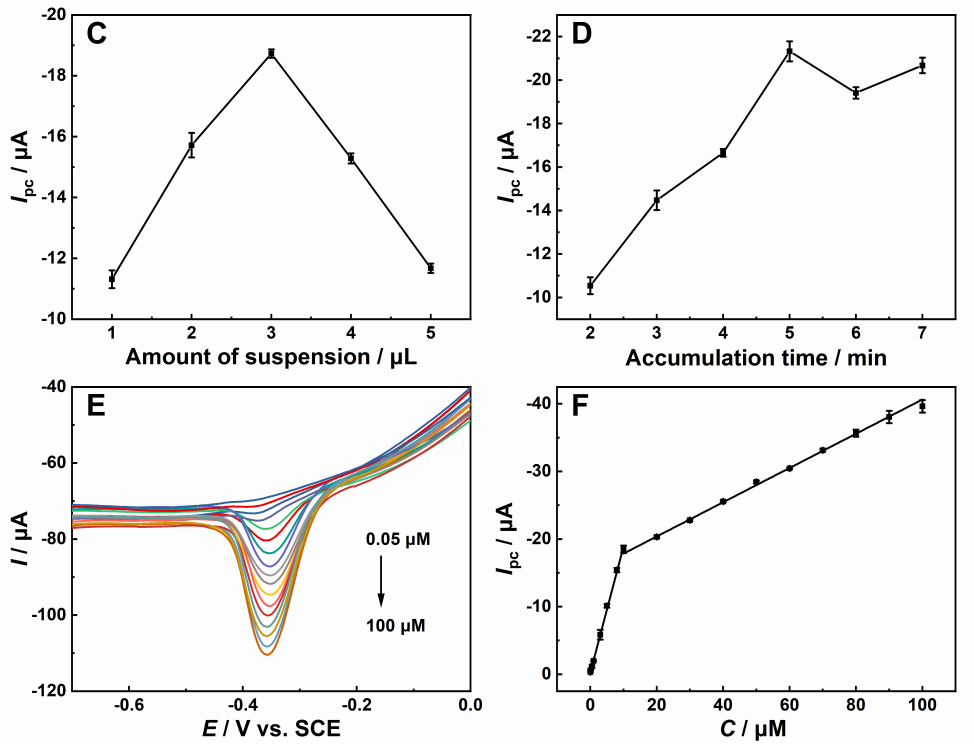

Fig. 7. (A) CVs of 100 μM NFT on a NiCo@C/FeCo@C@C modified GCE in 0.1 M PBS solutions with diverse pH values (scan rate: 100 mV s^{-1}). The insets are Linear fitting graphs of I_{pc} (I) or E_{pc} (II) with pH values. (B): CVs of 100 μM NFT on a NiCo@C/FeCo@C@C modified GCE at different scan rate (v). The insets are linear fitting graph of of I_{pc} and v (I) as well as calibration curve of E_{pc} *vs.* ln$v$ (II); The influence of the suspension amounts of NiCo@C/FeCo@C@C materials (C) and accumulation time (D) on the electrochemical signals of NFT. (E) DPVs at a NiCo@C/FeCo@C@C modified GCE under different NFT concentration; (F) I_{pc} vs. NFT concentration. Error bars represent the standard deviation of the mean from three sensors.

Scheme 2. The reduction mechanism for NFT on a NiCo@C/FeCo@C@C modified GCE.

Table 2. Comparison of a NiCo@C/FeCo@C@C modified GCE with other sensors

when applied for NFT quantitation.

Electrode	Linear range (μM)	LOD (nM)	Ref.
Ag-Ni $(OH)_2$	0.11-212	79	[38]
Cu_5Zn_8/HPCNC/SPE	0.75-473	311	[39]
$MgFe_2O_4$	0-342.6	33	[40]
f-CNF/CB/GCE	0.05-104.66	16	[41]
NPSC/GCE	1.0-2500	36	[42]
Ag/Se/GCE	0.1-210	23	[43]
NdM/SPCE	0.1-481	16	[44]
N-CQD@Co_3O_4/MWCNTs/GCE	0.05-1220	44	[45]
CTMs/GCE	10-140	21	[46]
Cu-TC4A-M@MC/GCE	4-1050	456	[47]
NiCo@C/FeCo@C@C/GCE	0. 05-100	14	This work

HPCNC: hollow porous carbon nanocubes; SPE: screen-printed electrode; f-CNF/CB: functionalized carbon nanofibers and carbon black hybrid composite; NPSC: N, P-hollow sphere carbon; NdM: neodymium molybdate; SPCE: screen printed carbon electrode; N-CQD: nitrogen-doped carbon quantum dots; MWCNTs: multi-walled carbon nanotubes; CTMs: calcium tungstate microspheres; Cu-TC4A-M@MC: two-dimensional thiacalix[4]arene-copper (I) MOF was mixed with mesoporous carbon.

The voltammetric quantification of NFT with NiCo@C/FeCo@C@C modified GCE was accomplished by differential pulse voltammetry (DPV) technique in PBS (0.1 M) supporting electrolyte (pH 7.0). The cathodic peak current (I_{pc}) generated from the reduction of NFT over NiCo@C/FeCo@C@C modified GCE amplified gradually with an increase of the NFT (Fig. 7E) concentration (C) from 0.05 to 100 μM. There were two linear ranges for the NFT detection on the NiCo@C/FeCo@C@C modified GCE. When the NFT concentration increases from 0.05 to 10 μM, the linear fitting equation of I_{pc} and C was I_{pc} (μA) = -1.865 C (μM) - 0.236 (R^2 = 0.994) (Fig. 7F). At higher concentrations from 10 to 100 μM, the linear regression equation was I_{pc} (μA) = -0.253 C (μM) - 15.310 (R^2 = 0.998). Additionally, the limit of detection (LOD) calculated from these voltammetric quantification for NFT was found to be as low as 14 nM with an error limit of 2.4%. Table 2 displays a comparative account of the linear ranges and LODs observed by NiCo@C/FeCo@C@C modified GCE with those reported electrochemical sensors

for NFT detection. This table evidently reveals that the sensing results from NiCo@C/FeCo@C@C modified GCE are either comparable or much better in the field of LOD and the linear range assessed for NFT.

The reproducibility, stability, and anti-interference capability of a NiCo@C/FeCo@C@C modified GCE toward the electrochemical sensing of NFT were explored. We investigate the reproducibility performance of NiCo@C/FeCo@C@C modified GCE sensor under the identical conditions. The RSD was evaluated using seven different electrodes. The current response signals at 10 μM NFT were examined for RSD calculations. The RSD value was 4.2%, indicating that the NiCo@C/FeCo@C@C modified GCE sensor displayed excellent reproducibility for sensing NFT (Fig. 8A). Stability is an essential indicator to assess the sensor performance. Therefore, the fabricated electrode was used to continuously monitor NFT every five days. When it was not in use, the developed sensor was stored at 4 . The electrochemical signal of the sensor changed slightly after one month, evidencing the prominent stability of the developed sensor toward the detection of NFT (Fig. 8B). In addition, the morphology of the sensing materials was investigated after the sensing experiment (the inset in Fig. 8B), and the SEM image shows that the cubic shape keeps, indicating the good stability of the sensor.

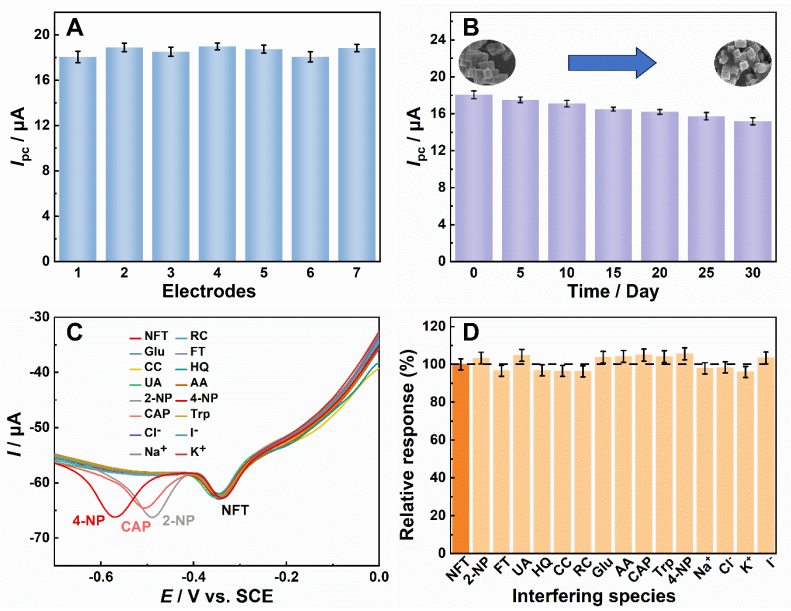

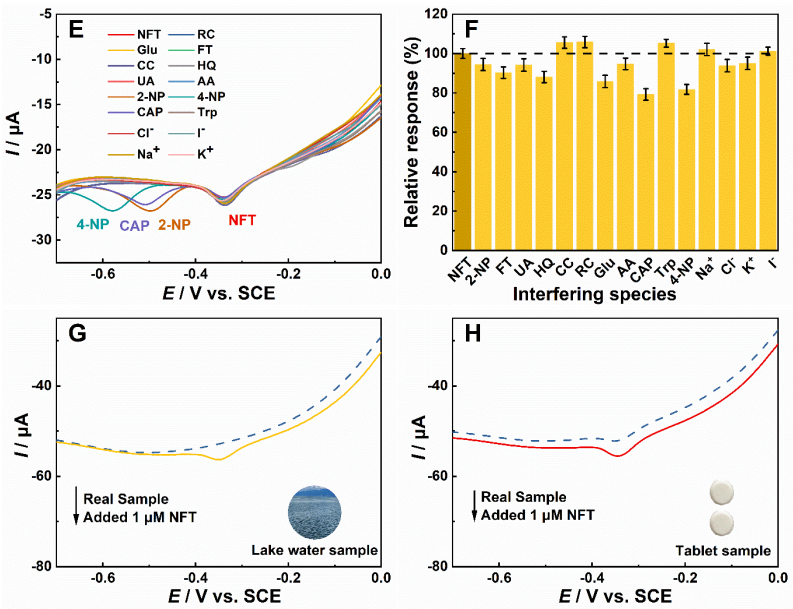

Fig. 8. (A) The electrochemical signals of seven various modified electrodes for the sensing of 10 μM NFT; (B) long-term stability of NiCo@C/FeCo@C@C modified GCE sensor every 5 days; (C,E) DPV curves of various interfering species and 2 μM NFT at a NiCo@C/FeCo@C@C (C) and a NiCo@C/FeCo@C (E) modified GCE in the 0.1 M PBS (pH 7.0); (D,F) The comparison of current responses before and after the addition of co-existing moieties during the NFT determination at a NiCo@C/FeCo@C@C (D) and a NiCo@C/FeCo@C (F) modified GCE. (G,H) DPV curves of lake water sample (G) or tablet sample (H) on a NiCo@C/FeCo@C@C modified GCE before and after the addition of NFT standard solutions. Error bars represent the standard deviation of the mean from three sensors.

In order to confirm the anti-interference capability of NiCo@C/FeCo@C@C modified GCE (Fig. 8C and 8D) and NiCo@C/FeCo@C modified GCE (Fig. 8E and 8F), 25 times concentration of 2-nitrophenol (2-NP), fructose (FT), uric acid (UA), hydroquinone (HQ), catechol (CC), resorcinol (RC), glucose (Glu), ascorbic acid (AA), chloramphenicol (CAP), tryptophan (Trp), 4-nitrophenol (4-NP) and 50 times concentration of Na^+, K^+, Cl^- and I^- were added into 2 μM NFT in 0.1 M PBS (pH 7.0), and the DPV curves were recorded, as shown in Fig. 8C and 8E. The electrochemical signal of NFT did not change much (lower than 10%) on NiCo@C/FeCo@C@C modified GCE (Fig. 8D), which fully proved that NiCo@C/FeCo@C@C modified GCE owned high anti-interference capability and could be utilized to practical determination. In comparison, the large influence on the electrochemical signal of NFT was observed on NiCo@C/FeCo@C modified GCE (Fig. 8F). This is mainly

due to the multi-core-shell nanoboxes with porous structure of NiCo@C/FeCo@C@C, which is benefit for the selectivity.

To explore and determine the practical applicability of the NiCo@C/FeCo@C@C sensor, for sensitive sensing of NFT, the DPV examinations over pharmaceutical (e.g., tablet) and lake water samples were accomplished in PBS (0.1 M) supporting electrolyte (pH 7.0) by the standard spiking method (Fig. 8G and 8H). Table 3 of the experimental results demonstrates that the constructed electrochemical sensor possesses suitable recovery rate for NFT determination in the real samples, based on the equation 1.

(**Equation 1**)

The NFT level in in the real samples was then detected and compared with that measured using high performance liquid chromatography (HPLC, Table 3). There was no obvious difference of the determined consequences, implying that the constructed NiCo@C/FeCo@C@C sensor owns a great potential in real sample analysis with high precision and accuracy.

Table 3. DPV measured results of NFT in tablet and lake water through HPLC and the GCE modified with NiCo@C/FeCo@C@C.

	Detection				Recovery test			
Sample	This method (μM)	RSD (%)	HPLC (μM)	RSD (%)	Spiked (μM)	Found (μM)	Recovery (%)	RSD (%)
Tablet	1.04 0.97 1.02	3.5	1.07 1.06 1.09	1.4	1	1.93 2.03 2.12	102.0	4.6
Lake water	ND	-	ND	-	1	1.03 0.96 1.05	102.0	4.3

4. Conclusions

In general, a highly efficient metal@carbon electrocatalyst with porous and multi-core-shell nanobox structure comprising PDA-derived C coated NiCo@C and FeCo@C nanohybrid (named as NiCo@C/FeCo@C@C) was fabricated by simply pyrolyzing NiCo@FeCo PBA@polydopamine. The NiCo@C/FeCo@C@C composite attained an enhanced electrochemical capability, such as outstanding electronic conductivity, a large number of active sites and a high electrocatalytic activity, which exhibited a highly sensitive response to NFT. Based on the novel

sensor fabricated by the NiCo@C/FeCo@C@C composite, the electrochemical behavior of NFT was investigated. The electrochemical determination approach occupied differential pulse voltammetry (DPV) and yielded a linear response in the range of 0.05-100 μM, coupled with low LOD of 14 nM. In addition, the established NiCo@C/FeCo@C@C electrochemical sensor also demonstrated good stability, high anti-interference ability, satisfactory reproducibility and practical application. This work paves a way for the development of highly efficient metal@carbon electrocatalyst with multi-core-shell structure for electrochemical sensing applications.

Acknowledgements

This work was financially supported by open project funding of Ministry of Education Key Laboratory for the Synthesis and Application of Organic Functional Molecules of Hubei University of China (No. KLSAOFM2302) and the Graduate Innovative Fund of Wuhan Institute of Technology of China. Thanks to eceshi (www.eceshi.com) for the TEM analysis.

The authors declare that they have no conflict of interest.

References

[1] N. Sivaraman, V. Duraisamy, L. Lucious, B, Saraswathyamma, S.M.S. Kumar, R. Thangamuthu, In-situ construction of N and P doped hollow sphere carbon for electrochemical sensing of antibiotic drug from poultry sustenance, Electrochim. Acta 441 (2023) 141773, https://doi.org/10.1016/j.electacta.2022.141773.

[2] R.K. Devi, M. Ganesan, T-W. Chen, S-M. Chen, A.M. Abbasi, M.A. Ali, M.S. Elshikh, J. Yu, H-Y. Chuang, B. Xu, S.K. Ravi, MXene-interdigitated holey-graphene oxide nanocomposite for simultaneous detection of antibiotic and anticancer drugs with ultra-high sensitivity, Chem. Eng. J. 474 (2023) 145693, https://doi.org/10.1016/j.cej.2023.145693.

[3] R.P. Dighole, A.V. Munde, B.B. Mulik, S.S. Zade, B.R. Sathe, Melamine functionalised multiwalled carbon nanotubes (M-MWCNTs) as a metal-free electrocatalyst for simultaneous determination of 4-nitrophenol and nitrofurantoin, New J. Chem. 46 (2022) 17272-17281,

https://doi.org/10.1039/D2NJ03901J.

[4] T-P. Sheng, C-Z. Sun, F-R. Dai, Triphenylamine-functionalized coordination cage as a supramolecular fluorescence sensor for sequential detection of aluminum ions and nitrofurantoin, ACS Appl. Mater. Interfaces 15 (2023) 29252-29258, https://doi.org/10.1021/acsami.3c01422.

[5] W. Fan, W. Gao, J. Jiao, D. Wang, M. Fan, Highly sensitive SERS detection of residual nitrofurantoin and 1-amino-hydantoin in aquatic products and feeds, Luminescence 37 (2022) 82-88, https://doi.org/10.1002/bio.4148.

[6] A.O. Melekhin, V.V. Tolmacheva, V.V. Apyari, S.G. Dmitrienko, Current trends in analytical strategies for the chromatographic determination of nitrofuran metabolites in food samples. An update since 2012, J. Chromatogr. A 1685 (2022) 463620, https://doi.org/10.1016/j.chroma.2022.463620.

[7] M. Li, T. Zhe, F. Li, R. Li, F. Bai, P. Jia, T. Bu, Z. Xu, L. Wang, Hybrid structures of cobalt-molybdenum bimetallic oxide embedded in flower-like molybdenum disulfide for sensitive detection of the antibiotic drug nitrofurantoin, J. Hazard. Mater. 435 (2022) 129059, https://doi.org/10.1016/j.jhazmat.2022.129059.

[8] H. Gu, X. Shui, Y. Zhang, T. Zeng, J. Yang, Z. Wu, X. Zhang, N. Yang, Porous carbon scaffolded Fe-based alloy nanoparticles for electrochemical quantification of acetaminophen and rutin, Carbon 221 (2024) 118954, https://doi.org/10.1016/j.carbon.2024.118954.

[9] P. Liu, Y. Zhang, L. Ye, M. Huang, T. Zeng, J. Yang, F. Tian, Z. Wu, X. Zhang, C. Hu, N. Yang, Laser-induced graphene decorated with Ni-Pt alloy nanoparticles for non-enzymatic electrochemical quantification of glucose, Diam. Relat. Mater. 146 (2024) 111205, https://doi.org/10.1016/j.diamond.2024.111205.

[10] Y. Zou, H. Gu, J. Yang, T. Zeng, J. Yang, Y. Zhang, A high sensitivity strategy of nitrite detection based on CoFe@NC nanocubes modified glassy carbon electrode, Carbon Lett. 33 (2023) 2075-2086, https://doi.org/10.1007/s42823-023-00558-4.

[11] X. Hu, Y. Zhang, T. Zeng, Q. Wan, K. Wu, N. Yang, A novel electrochemical sensor based on MnOOH nanorod/expanded graphite for sensitive monitoring of metronidazole, Diam. Relat. Mater. 128 (2022) 109303, https://doi.org/10.1016/j.diamond.2022.109303.

[12] M. Cao, Y. Zou, Y. Zhang, T. Zeng, Q. Wan, G. Lai, N. Yang, Robust and selective electrochemical sensing of hazardous photographic developing agents

using a MOF-derived 3D porous flower-like Co_3O_4@C/graphene nanoplate composite, Electrochim. Acta 409 (2022) 139967, https://doi.org/10.1016/j.electacta.2022.139967.

[13] J. Peng, Q. Huang, W. Zhuge, Y. Liu, C. Zhang, W. Yang, G. Xiang, Blue-light photoelectrochemical sensor based on nickel tetra-amined phthalocyanine-graphene oxide covalent compound for ultrasensitive detection of erythromycin, Biosens. Bioelectron. 106 (2018) 212-218. https://doi.org/10.1016/j.bios.2018.02.009.

[14] J. Peng, Q. Huang, Y. Liu, P. Liu, C. Zhang, Photoelectrochemical sensor based on composite of CdTe and nickel tetraamined phthalocyanine covalently linked with graphene oxide for ultrasensitive detection of curcumin, Sensor. Actuator. B: Chem. 294 (2019) 157-165. https://doi.org/10.1016/j.snb.2019.05.047.

[15] G. Xiang, X. He, Y. Liu, Q. Huang, W. Huang, C. Zhang, J. Peng, A sensitive photoelectrochemical sensor for levodopa detection using benzothiadiazole-based conjugated microporous polymer-coated graphene heterostructures, ACS Appl. Mater. Interfaces 14 (2022) 51329-51340. https://doi.org/10.1021/acsami.2c15516.

[16] R. Karthik, R. Sukanya, P.R. Chavan, M. Hasan, E. Kamaraj, C.B. Breslin, J. Lee, J-J. Shim, Temperature-induced conversion of 2D vanadium-doped $MoSe_2$ nanosheets to 1D V_2MoO_8 rods: Enhanced performance in electrochemical antibiotic detection in biological and environmental samples, ACS Appl. Mater. Interfaces 16 (2024) 29374-29389, https://doi.org/10.1021/acsami.4c02022.

[17] V. Vinothkumar, R. Sakthivel, S-M. Chen, A. Sangili, T.H. Kim, Construction of Sr@Mn_3O_4/GO nanocomposite: A synergistic electrocatalyst for nitrofurantoin detection in biological and environmental samples, Environ. Sci-Nano. 10 (2023) 503-518, https://doi.org/10.1039/D2EN00983H.

[18] G. Mukundan, S. Badhulika, Composite of a stabilizer-free trimetallic prussian blue analogue (PBA) and polyaniline (PANI) on 3D porous nickel foam for the detection of nitrofurantoin in biological fluids, ACS Appl. Bio. Mater. 7 (2024) 2924-2935, https://doi.org/10.1021/acsabm.3c01297.

[19] S.B. Ravikumar, S.B. Prasanna, S.A. Shivamurthy, S. Shadakshari, B.M. Nagaraja, J.R. Rajabathar, S. Arokiyaraj, Individual and simultaneous electrochemical determination of nitrofurantoin and ascorbic acid in biological samples using a novel La_2YBiO_6 double perovskite deposited on MWCNTs as a

nanocomposite, New J. Chem. 47 (2023) 21307-21317, https://doi.org/10.1039/D3NJ04573K.

[20] R.D. Nagarajan, V. Magesh, A.K. Sundramoorthy, P. Murugan, R. Atchudan, D. Ganapathy, S. Arya, A.M. Karami, M. Govindasamy, Graphene nanoribbons/ manganese oxide nanocomposite modified electrode for detection of antimicrobial drug nitrofurantoin, J. Nanomater. 13 (2023) 5484059, https://doi.org/10.1155/2023/5484059.

[21] S.H. Tumrani, R.R. Neiber, Z. Pitafi, I.A. Ahmed, R.A. Soomro, M.M. Ibrahim, S. Karakus, Z.M. El-Bahy, Synergistic integration of few-layer thick MXenes and small Pd nanocubes for enhanced electrochemical nitrofurantoin detection: Implications in pharmaceutical pollutant monitoring, J. Environ. Chem. Eng. 11 (2023) 111152, https://doi.org/10.1016/j.jece.2023.111152.

[22] A.T.E. Vilian, S-K. Hwang, G. Bhaskaran, M. Alhammadi, S. Kim, J.N. Tiwari, Y.S. Huh, Y-K. Han, Polypyrrole-MXene supported gold nanoparticles for the trace-level detection of nitrofurantoin, Chem. Eng. J. 454 (2022) 139980, https://doi.org/10.1016/j.cej.2022.139980.

[23] M. Li, T. Zhe, R. Li, F. Bai, P. Jia, Z. Xu, X. Wang, T. Bu, H. Wu, L. Wang, ZIF-derived Co nanoparticles embedded into N-doped carbon nanotube composites for highly efficient electrochemical detection of nitrofurantoin in food, Food Chem. 418 (2023) 135948, https://doi.org/10.1016/j.foodchem.2023.135948.

[24] M. Chu, Y. Wang, J. Xin, D. Chu, Y. Liu, D. Song, G. Yang, H. Ma, H. Pang, X. Wang, Preparation of a three-dimensional bimetallic $CoFe_x$/ N-doped carbon nanomaterial used as modified electrode for the efficient electrochemical detection of L-tyrosine, Mater. Chem. Phys. 315 (2024) 129003, https://doi.org/10.1016/j.matchemphys.2024.129003.

[25] Y. Li, X. Liu, J. Zheng, A dual-ratiometric electrochemical sensor based on Cu/N-doped porous carbon derived from Cu-metal organic framework for acetaminophen determination, Microchem. J. 189 (2023) 108556, https://doi.org/10.1016/j.microc.2023.108556.

[26] M. Pappathi, P. Vajeeston, A.S.S. Raja, A. Vignesh, A. Syed, A.H. Bahkali, L. Cathrine, J.A. Sekar, A. Roveena, S-M. Phang, G.G. Kumar, Trimetallic ZIF-derived Ni-Cu/NC rhombic dodecahedron nanostructures on butter sheet paper as a flexible electrochemical probe for nonenzymatic glucose sensors, ACS Appl. Nano Mater. 6 (2023) 14628-14644,

https://doi.org/10.1021/acsanm.3c01489.

[27] L. Zhang, J. Li, Y. Yang, C. Wang, Y. Wang, P. Zhao, Y. Xie, J. Fei, A novel electrochemical sensor based on mesoporous carbon hollow spheres/ZIF-67-derived Co-embedded N-doped carbon nanotubes composite for simultaneous determination of dihydroxybenzene isomers in environmental water samples, Microchem. J. 191 (2023) 108754, https://doi.org/10.1016/j.microc.2023.108754.

[28] S.A. Hira, S. Nagappan, M. Yusuf, A.C. Chen, J-M. Lee, K.H. Park, L-Cysteine anchored Co-MOF derived cobalt-nitrogen-carbon hierarchical architecture as an efficient sensor for the electrochemical detection of catecholamine, Microchem. J.190 (2023) 108748, https://doi.org/10.1016/j.microc.2023.108748.

[29] Y. Qin, D. Xiao, X. Gao, X. Zhang, Y. Xu, Nanocubic cobalt-containing prussian blue analogue-derived carbon-coated CoFe alloy nanoparticles for noninvasive uric acid sensing, Anal. Methods 16 (2024) 2496-2504, https://doi.org/10.1039/D4AY00121D.

[30] Y. Niu, Y. Li, F. Ma, M. Zhang, X. Chen, B-C. Ye, Ratiometric electrochemical sensing platform based on N-doped MOF-derived CoNi/C for the determination of p-phenylenediamine in hair dyes, Microchim. Acta 190 (2023) 22, https://doi.org/10.1007/s00604-022-05600-2.

[31] G. Xie, G. Li, D. Chen, X. Meng, C. Fan, B. Pang, Y. Zhang, Y. Chen, L. Yu, L. Dong, Highly sensitive non-enzymatic glucose sensor based on CoCu@MC derived from CoCu/melamine cyanurate superstructures, Diam. Relat. Mater. 130 (2022) 109509, https://doi.org/10.1016/j.diamond.2022.109509.

[32] Z. Zhang, F. Shi, Y. Ai, X. Li, D. Zhang, L. Wang, W. Sun, Portable wireless electrochemical sensing of breviscapine using core-shell ZIFs-derived Co nanoparticles embedded in N-doped carbon nanotube polyhedra-modified electrode, Microchim. Acta 191 (2024) 290, https://doi.org/10.1007/s00604-024-06298-0.

[33] Y. Wei, M. Z, W. Zhu, H. Pang, Hollow structures prussian blue, its analogs, and their derivatives: Synthesis and electrochemical energy-related applications, Carbon Neutralization 2 (2023) 271-299, https://doi.org/10.1002/cnl2.64.

[34] J-Z. Chen, B-Y. Lei, Y-L. Hou, J-T. Lei, P-P. Chen, Z-A. Li, D-L. Zhao, Graphene aerogel encapsulated double carbon shell CoFe@C@C nanocubes for construction of high performance microwave absorbing materials, Carbon 224

(2024) 119081, https://doi.org/10.1016/j.carbon.2024.119081.

[35] H. Zhang, J. Diao, M. Ouyang, H. Yadegari, M. Mao, M. Wang, G. Henkelman, F. Xie, D.J. Riley, Heterostructured core−shell Ni−Co@Fe−Co nanoboxes of prussian blue analogues for efficient electrocatalytic hydrogen evolution from alkaline seawater, ACS Catal. 13 (2023) 1349-1358, https://doi.org/10.1021/acscatal.2c05433.

[36] Y. Wang, L. Zhu, J. Wang, Z. Zhang, J. Yu, Z. Yang, Enhanced chemisorption and catalytic conversion of polysulfides via CoFe@NC nanocubes modified separator for superior Li–S batteries, Chemical Engineering Journal 433 (2022) 133792, https://doi.org/10.1016/j.cej.2021.133792.

[37] F. Wang, N. Wang, X. Han, D. Liu, Y. Wang, L. Cui, P. Xu, Y. Du, Core-shell FeCo@carbon nanoparticles encapsulated in polydopaminederived carbon nanocages for efficient microwave absorption, Carbon 145 (2019) 701-711, https://doi.org/10.1016/j.carbon.2019.01.082.

[38] M. Ezazi, K. Asadpour-Zeynali, E. Saeb, Synergistic incorporation of Ag into nickel hydroxide nanostructure to enhance the electroctrocatalytic determination of nitrofurantoin, Inorg. Chem. Commun. 160 (2024) 111913, https://doi.org/10.1016/j.inoche.2023.111913.

[39] R. Sakthivel, T-Y. Liu, R-J. Chung, Bimetallic Cu_5Zn_8 alloy-embedded hollow porous carbon nanocubes derived from 3D-Cu/ZIF-8 as efficient electrocatalysts for environmental pollutant detection in water bodies, Environ. Res. 216 (2023) 114609, https://doi.org/10.1016/j.envres.2022.114609.

[40] J.N. Baby, B. Sriram, S-F. Wang, M. George, Effect of various deep eutectic solvents on the sustainable synthesis of $MgFe_2O_4$ nanoparticles for simultaneous electrochemical determination of nitrofurantoin and 4-nitrophenol, ACS Sustainable Chem. Eng. 8 (2020) 1479-1486, https://doi.org/10.1021/acssuschemeng.9b05755.

[41] A.S. Haidyrah, P. Sundaresan, K. Venkatesh, S.K. Ramaraj, B. Thirumalraj, Fabrication of functionalized carbon nanofibers/carbon black composite for electrochemical investigation of antibacterial drug nitrofurantoin, Colloid. Surface. A. 627 (2021) 127112, https://doi.org/10.1016/j.colsurfa.2021.127112.

[42] N. Sivaraman, V. Duraisamy, L. Lucious, B. Saraswathyamma, S.M.S. Kumar, R. Thangamuthu, In-situ construction of N and P doped hollow sphere carbon for electrochemical sensing of antibiotic drug from poultry sustenance, Electrochim.

Acta 441 (2023) 141773, https://doi.org/10.1016/j.electacta.2022.141773.

[43] A.J.J. Amalraj, U.N. Murthy, S-F. Wang, Silver-capped selenium explored as an electro-catalyst for simultaneous detection of nitro-aromatic drugs in different aqueous samples, J. Ind. Eng. Chem. 108 (2022) 243-253, https://doi.org/10.1016/j.jiec.2022.01.004.

[44] J.V. Kumar, R. Karthik, S-M. Chen, K-H. Chen, S. Sakthinathan, V. Muthuraj, T-W. Chiu, Design of novel 3D flower-like neodymium molybdate: An efficient and challenging catalyst for sensing and destroying pulmonary toxicity antibiotic drug, Chem. Eng. J. 346 (2018) 11-23, https://doi.org/10.1016/j.jiec.2022.01.004.

[45] G. Muthusankar, R. Devi, G. Gopu, Nitrogen-doped carbon quantum dots embedded Co_3O_4 with multiwall carbon nanotubes: An efficient probe for the simultaneous determination of anticancer and antibiotic drugs, Biosens. Bioelectron. 150 (2020) 111947, https://doi.org/10.1016/j.bios.2019.111947.

[46] P. Manikanta, Mounesh, R.R. Nikam, S. Sandeep, B.M. Nagaraja, Development of novel microsphere structured-calcium tungstate as efficacious electrocatalyst for the detection of antibiotic drug nitrofurantoin, J. Mater. Chem. B 11 (2023) 11600, https://doi.org/10.1039/D3TB02087H.

[47] L. Ma, W-Y. Pei, H-L. Xu, J. Yang, J-F. Ma, Composite of a thiacalix[4]arene-copper(I) metal-organic framework and mesoporous carbon for efficient electrochemical detection of antibiotics, Talanta 269 (2023) 125490, https://doi.org/10.1016/j.talanta.2023.125490.